CrossMark

Flame synthesized Y_2O_3:Tb^{3+}–Yb^{3+} phosphors as spectral convertors for solar cells

Sovann Khan[1,2] · Bo-In Park[1] · Joon Soo Han[1] · Seung Yong Lee[1,2] · So-Hye Cho[1,2]

Abstract Near-infrared (NIR) quantum cutting phosphors serve as a potential material for fabricating photovoltaic spectral convertors. In many cases, quantum cutting phosphors are obtained via a wet chemical method coupled with a post-annealing treatment—a very costly process. In this report, we used continuous flame spray pyrolysis (FSP) for fabricating Y_2O_3:Tb^{3+}–Yb^{3+} quantum-cutting phosphors without any post-treatment. Based on characterizations by scanning electron microscopy, transmission electron microscopy, and X-ray diffraction, we found that as-synthesized Y_2O_3:Tb^{3+}–Yb^{3+} phosphors exhibit hollow and shell-like micro-structures composed of highly crystalline and pure cubic-phase nanoparticles (< 50 nm). Photoluminescence studies of the phosphors revealed that NIR emissions appeared with the introduction of Yb to Y_2O_3:Tb^{3+}. Phosphor size was successfully controlled by managing the concentration of the metal precursor solution for FSP. The Y_2O_3:Tb^{3+}–Yb^{3+} phosphors were then embedded into transparent poly-ethylene-*co*-vinyl acetate (EVA) film to form a spectral convertor. The composite films of Y_2O_3:Tb^{3+}–Yb^{3+} phosphors and poly-EVA were found to be highly transparent in the visible range (> 500 nm), making them suitable as spectral photovoltaic convertors.

✉ So-Hye Cho
  sohyec@kist.re.kr

1 Materials Architecturing Research Center, Korea Institute of Science and Technology, Hwarangno 14-gil 5, Seongbuk-gu, Seoul 02792, Republic of Korea

2 Division of Nano & Information Technology, Korea University of Science and Technology, 217 Gajeong-ro Yuseong-gu, Daejeon 34113, Republic of Korea

Introduction

Year by year, the climate change due to the global warming is threatening every life on the earth. Using fossil fuel for an energy supply accounts for one of the reasons for the climate change because a great amount of CO_2 gas is emitted from the fossil combustion. To save the earth from the global warming, utilization of renewable energy has been discussed. A solar cell is considered as a green technology since it harvests energy from the sunlight. Among different kinds of solar cell devices, the crystalline silicon solar cell is most widely used and takes 90% of the world's solar cell market, according to ACS C&EN news (2016) [1]. Although, there is unlimited energy from the sunlight, the conversion efficiency of light to electricity of a solar cell is still low. The latest report in 2016 showed that the highest efficiency of crystalline silicon solar cell module reached ~ 25.6% by the Panasonic HIT (heterojunction with intrinsic thin layer) solar panel [2]. The main problem in this low efficiency of solar cells is that with one kind of a solar cell, it is difficult to absorb all sunlight spanning ultraviolet to infrared radiations. Therefore, higher energy than the bandgap of a solar cell is lost by thermalization while lower energy is lost by transmission. To overcome this intrinsic problem, applying a spectrum convertor to a solar cell is considered as a very promising approach for increasing solar cell performance [3].

Near-infrared quantum cutting phosphors (NIR-QCs) are among excellent luminescent materials for the spectral convertor since they make it possible to emit two NIR photons from one UV/visible photon absorption, resulting in a quantum efficiency as high as 200% [4]. Phosphors composed of an Y_2O_3 host and lanthanide dopants have drawn a great interest due to their high chemical and thermal stability and excellent luminescent properties. The Y_2O_3 phosphor dually doped with Tb^{3+} and Yb^{3+} (designated as Y_2O_3:Tb^{3+}–Yb^{3+} below) is an excellent candidate for a spectral convertor in solar cell applications since the emission energy from Yb^{3+} ions in this phosphor matches well with the bandgap energy of the Si semiconductor ($E_g = 1.12$ eV, $\lambda = 1100$ nm) [3, 5]. In order to apply the Y_2O_3:Tb^{3+}–Yb^{3+} phosphor for a spectral convertor, control of its particle size is important. A spectral convertor, especially the down-converting layer, requires having a high transmittance since it is located on top of a solar cell device (facing the Sun). Therefore, to obtain a transparent layer with the Y_2O_3:Tb^{3+}–Yb^{3+} phosphor, the size of the phosphor needs to be controlled small enough to avoid light scattering and also it has be well dispersed in a highly transparent polymer matrix [6].

Wet chemical methods are commonly used to fabricate nano-sized particles [7, 8]. We have also successfully synthesized Y_2O_3:Tb^{3+}–Yb^{3+} nanoparticles by the co-precipitation method followed by a post-annealing [5]. However, wet chemical methods take a long time and produce much waste, and the optical properties of the resulting product are not guaranteed unless a thermal treatment at high temperature is applied. Due to both high energy consumption and environmental concerns, wet chemical methods do not appeal for the large scale-production in the industry.

Flame spray pyrolysis (FSP) is a highly productive way to obtain powders in high crystallinity and purity. The process runs with liquid precursors (either concentrated

or diluted in a solvent) and the precursors are spayed into small droplets which are treated with a high temperature flame, up to 3000 °C. Controlling the flame temperature profile (determined by burner configuration, precursor composition and oxidant/fuel flow rates) and precursor concentration, synthesis of particles with different characteristics (e.g., size, morphology and phase) can be realized [9]. The process is very quick and the obtained products are often highly crystalline due to the high temperature of the flame. In addition, it can be operated continuously making it suitable for industrial production [10, 11]. Therefore, FSP is quite applicable for high quality phosphor materials and has been previously applied for phosphor synthesis by several research groups [12, 13]. For an example, Pratsinis et al., reported the synthesis of Y_2O_3:Eu^{3+} nanophosphor by FSP [14]. By controlling the residence time in the flame, they were able to obtain highly crystalline phosphors without post-treatment [14, 15].

In this report, we successfully synthesized Y_2O_3:Tb^{3+}–Yb^{3+} nanoparticles by FSP. We found that the particle size can be easily controlled by the dilution of precursor solution. The obtained product was highly crystalline and showed the quantum-cutting emission without a post-annealing process. To fabricate the phosphor product as a spectral convertor, polyethylene–vinyl acetate (EVA) film was used. The poly-EVA is the copolymer of ethylene and vinyl acetate and is industrially applied for encapsulating a solar cell between a front glass and a backsheet due to its strong adhesive properties and high transparency (over 90% transmittance in the visible light). Based on these properties, poly-EVA film was chosen as a matrix in this study for embedding nano-phosphors and thereby forming a spectral convertor for a solar cell.

Experimental

Y_2O_3:Tb^{3+}–Yb^{3+} synthesis

Precursor preparation

Metal nitrate hydrates such as $Y(NO_3)_3 \cdot 6H_2O$ (Alfa Aesar, 99.9%), $Yb(NO_3)_3 \cdot 6H_2O$ (Alfa Aesar, 99.99%), and $Tb(NO_3)_3 \cdot 6H_2O$ (Alfa Aesar, 99.999%) were used as starting precursors. The starting precursors were dissolved in ethanol by a magnetic stirring for 2 h in an ambient condition. Doping concentration of Tb was fixed at 1 mol% because the optimum concentration of Tb^{3+} single doping for the green luminescence was found to be about 1% [5]. Yb content was varied from 0 to 10 mol% in respect to Y. The total concentrations of precursors were varied from 0.05 to 0.001 M by serial dilution with ethanol.

FSP experimental set-up

The set-up for FSP was modified from our previous report [16] and a simplified diagram is drawn in Fig. 1. An atomizing spray nozzle was purchased from

Fig. 1 Schematic diagram of FSP experimental set-up
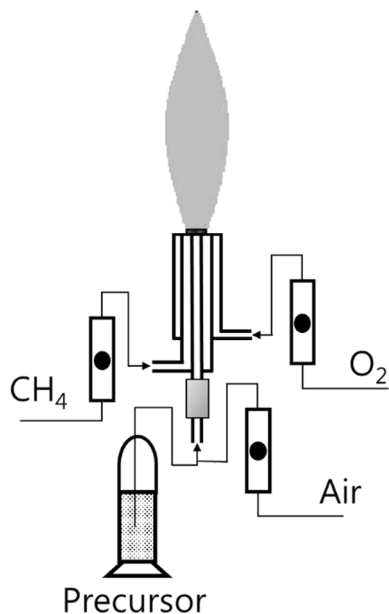
Daewoo Precision Co. and equipped with a diffusion-type burner (SUS 304, home-made, inner-diameter of 6 cm, outer-diameter of 8 cm, and length of 11 cm). The precursor solution was sprayed by the constant air pressure at 4 bars and its feeding speed was 30 mL/min. CH_4 (flow rate = 6 L/min) and O_2 (flow rate = 24 L/min) were used as a fuel and an oxidizer to generate the flame. All fluid flow rates were controlled by flow meters (RMA-12-SSV, Dwyer Instruments Inc.). Droplets produced from the spray nozzle passed through the flame of the burner (max. temperature = approx. 1250 °C, measured by R-type thermocouple) with a residence time less than 0.6 s. The exothermal pyrolysis took place and formed particles were collected on a metal mesh filter. The obtained powder was subjected for characterizations without any post-treatment.

Fabrication of EVA film

The EVA film was synthesized by the casting and drying method, modified from the method reported by Zhou et al. [17]. The EVA powder (1 g, Sigma Aldrich) was dissolved into 10 mL of chloroform (Sigma Aldrich, > 99.8%) to form an EVA solution. Different amounts (5, 10, and 20 mg) of Y_2O_3:$Tb^{3+}$$Yb^{3+}$ particulate phosphors were dispersed into the EVA solution. The colloidal solution were sonicated for 30 m and mixed at room temperature by magnetic stirring for 2 h. Then, the colloidal solution was poured into a glass petri dish (diameter of 10 cm) and dried in a vacuum oven at 40 °C for 24 h.
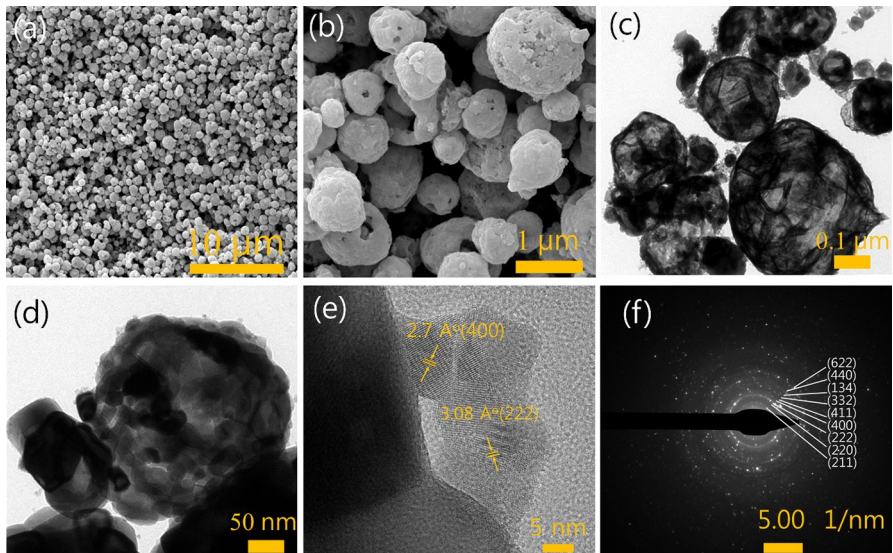
Characterizations

Morphological observation of particles and films was conducted by field emission scanning electron microscopy (FESEM) (Inspect F50, FEI Company). Nano-structures of particles were observed by high resolution scanning/transmission electron microscopy (S/TEM) (Talos F200X, FEI Company) and elemental mapping was obtained by energy dispersive X-ray spectroscopy (EDS) (Talos F200X, FEI Company). Crystal structure was studied by X-ray diffraction (XRD) (D8 Advanced, Brucker Corporation). The optical properties of synthesized products such as photoluminescence (PL), photoluminescence excitation (PLE) and decay time were evaluated by using two spectrophotometers (USB4000, Ocean Optics for NIR emission and F-7000, Hitachi Inc. for visible emission). Optical transmittance of luminescent films was obtained by an UV–visible Spectrophotometer (Varian Cary 100, Agilent Technologies).

Result and discussion

Structural properties of Y_2O_3:$Tb^{3+}Yb^{3+}$

The initial product was obtained with the precursor solution of 1 mol% Tb and 3 mol% Yb at the total concentration of 0.05 M. The overall morphology of the as-synthesized products was observed with SEM images which are shown in
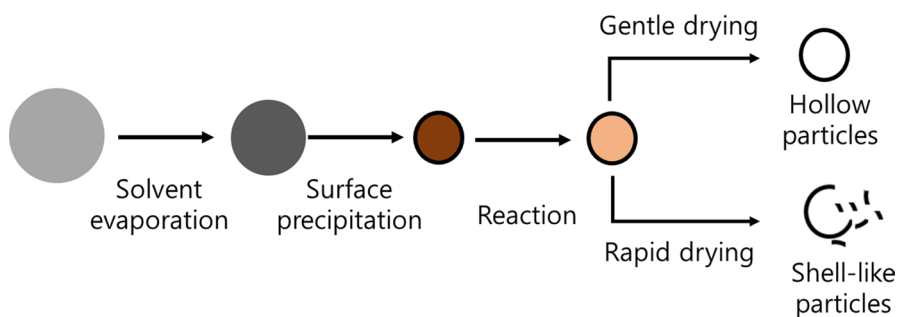

Fig. 2 **a**, **b** SEM images at the magnification of ×3000 and ×20,000, respectively; **c**, **d** TEM images at the magnification of ×15,000 and ×29,000, respectively; **e** a high-resolution TEM image; **f** a SAED pattern
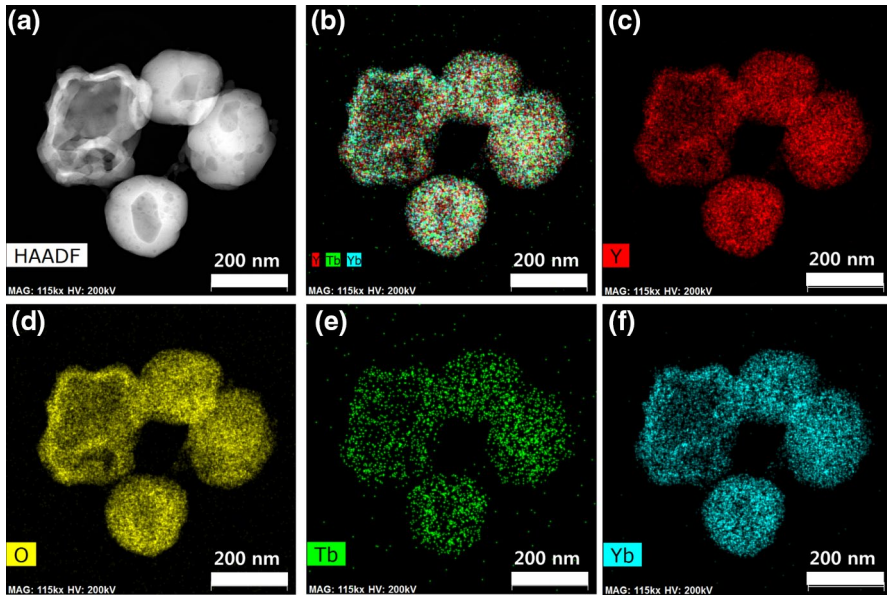
Fig. 2a, b. Non-aggregated spherical particles with poly-dispersed sizes rang-
ing from 0.1 to 6 μm were observed, and the spherical particles appeared to be
porous. The further observation of the particle by TEM revealed that each parti-
cle was not a dense particle but an aggregate of many fine particles (avg. particle
size: < 50 nm) forming a hollow/shell-like micro-structure (Fig. 2c, d). Highly
crystalline nature of the fine particles was proven by a high resolution TEM
image (Fig. 2e) showing well-defined lattice distances of ~ 2.7 and 3.08 Å which
correspond to planes (400) and (222) of cubic Y_2O_3 phase, respectively (accord-
ing to JCPDS#71-0099). A selected area electron diffraction (SAED) pattern fur-
ther supported a small size but a highly crystalline nature of the product (Fig. 2f).

The spherical shape of particles is quite common by FSP due to the natural
spherical shape of precursor droplets [9]. However degrees of agglomeration and
coalescence differ by the precursor and flame conditions. In our experiment, we
used the nitrate metal complexes and ethanol as precursors which are ignitable
and generate high enthalpy by combustion. Therefore, the complete combustion
of precursors was possible by a rather small flame. The hollow/shell-like micro-
structure was presumably formed due to nucleation/precipitation of fine parti-
cles preferentially on the surface rather than inside the droplets. The broad size
distribution (0.1–6 μm) might be the reason for the mixed morphologies of the
hollow and shell-like structures since the hollow spheres were found with bigger
particles (probably due to the rather slow drying caused by the big size) and the
shell-like particles were observed with smaller ones (due to the rather fast dry-
ing), which is in good agreement with [9]. A possible formation mechanism of
the hollow/shell-like particles by FSP is summarized in Scheme 1.

Elemental mapping of the spherical particles was provided by EDS showing
even distribution of all elemental compositions such as Y, O, Yb and Tb indicat-
ing well dispersed dopants (Tb^{3+} and Yb^{3+}) into the Y_2O_3 crystals (Fig. 3). Dop-
ing contents of Tb and Yb obtained from EDS were ~ 0.95 and 3.14%, respec-
tively, which are close to the theoretical composition.

Scheme 1 A possible mechanism of spherical hollow-shell particles by FSP, referenced from [9]
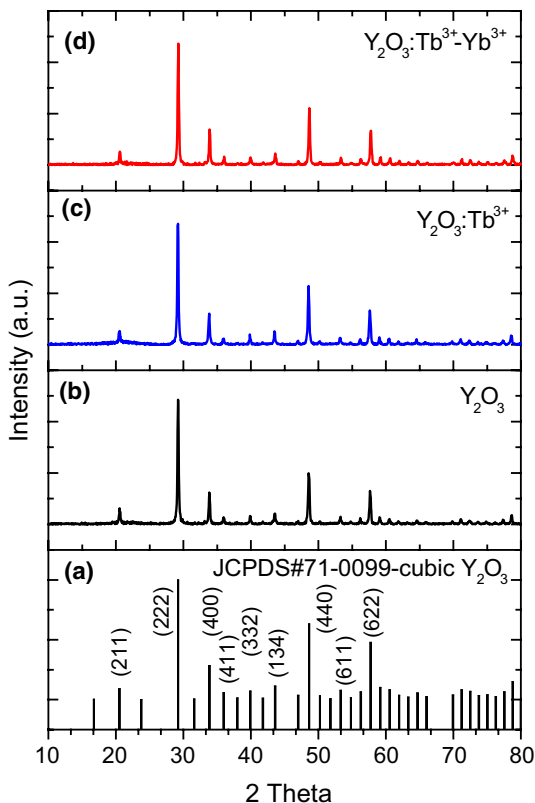
Fig. 3 Elemental mappings of FSP-synthesized Y_2O_3:Tb^{3+}–Yb^{3+} with a molecular composition of 96, 1 and 3 for Y^{3+}, Tb^{3+} and Yb^{3+} respectively: **a** STEM; **b** total elements mapping; and **c–f** individual element mapping (**c** Y; **d** O; **e** Tb; and **f** Yb). (Color figure online)

Crystalline structures of FSP products

The crystal structure of Y_2O_3:Tb^{3+}–Yb^{3+} synthesized by FSP with a total precursor concentration of 0.05 M was characterized by the XRD patterns. It showed that all products, regardless of doping, were obtained as a pure cubic phase of Y_2O_3 (Fig. 4). The intense XRD peaks at 20.542°, 29.21°, 33.87°, 35.98°, 39.93°, 43.58°, 48.63°, 53.28° and 57.74° are well identified as planes of (211), (222), (400), (411), (332), (134), (440), (611) and (622), respectively, of cubic Y_2O_3 (according to JCPDS#71-0099). Doping of 1 mol% Tb and Tb–Yb codoping (1 and 3 mol% respectively) neither caused any formation of impurity phases nor altered the peak position and shape. As a flame temperature is very high (as high as 3000 °C) and cooling rates are fast, the FSP process often results in the formation of metastable states of solids that are not possible to obtain by conventional wet synthesis or calcination. Therefore, synthesis of a monoclinic phase, a metastable phase of Y_2O_3, has been reported by the FSP process. For an example, Kang et al. [18] obtained a pure monoclinic phase of Y_2O_3:Eu^{3+} when the high temperature FSP was applied (typically using propane and hydrogen as a fuel can provide high temperatures above 2000 °C) and they reported that the monoclinic phase transformed to the cubic phase after post-annealing at 1200 °C. However, in our FSP condition, only the cubic phase was formed, probably due to the relatively low temperature of the flame, 1250 °C (measured by a R-type thermocouple).

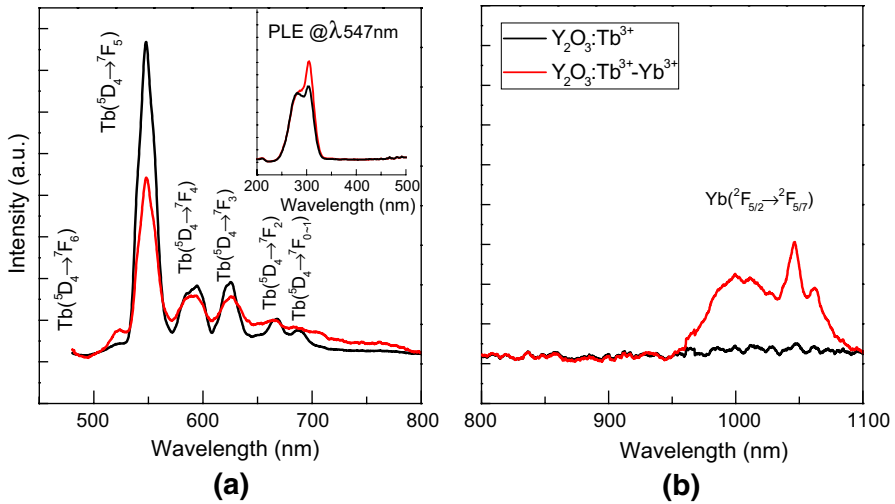**Fig. 4** XRD profiles of *a* Y_2O_3 JCPDS, *b* Y_2O_3, *c* Y_2O_3:1 mol%Tb^{3+}, and *d* Y_2O_3:1 mol%Tb^{3+}–3 mol%Yb^{3+}

Luminescence properties of Y_2O_3:$Tb^{3+}Yb^{3+}$ particles

Photoluminescence spectra of Y_2O_3:Tb^{3+} and Y_2O_3:Tb^{3+}–Yb^{3+} particles were examined for the Tb green emission and the quantum cutting emission by an energy transfer from Tb to Yb. With the excitation of 365 nm, Y_2O_3:Tb^{3+} (1 mol% doping) particles provided the green emissions which correspond well to the electronic transitions of Tb^{3+} ($^5D_4 \rightarrow {}^7F_J$ (J = 5, 4, 3, 2 and 1)) with the most intense peak at 547 nm (J = 5) and minor peaks at λ = 590, 623 and 660 and 690 nm. The electronic transition of $^5D_4 \rightarrow {}^7F_6$ at ~ 482 nm was not recorded due to the use of a cut-off filter (λ < 500 nm); the use of which was necessary to remove the source peak (Fig. 5a) [5, 19]. The excitation spectra of Y_2O_3:Tb^{3+} monitoring $^5D_4 \rightarrow {}^7F_5$ transition at 547 nm showed a broad peak at around λ = 250–350 nm (most intense at λ = 300 nm) and small peaks at around λ = 485 nm (Fig. 5a inset). The major excitation peak corresponds to the spin-allowed 4f–5d bands of Tb and the minor peaks to the spin-forbidden 4f–5d bands. A charge transfer peak of O^{2-}–Tb^{3+} in Y_2O_3 (typically observed at very high energy (λ < 250 nm) [20]) was not found informing us that all emissions are attributed to the 5d–4f transitions of Tb. When 3 mol% of Yb was co-doped into the Y_2O_3:Tb^{3+} phosphor, under
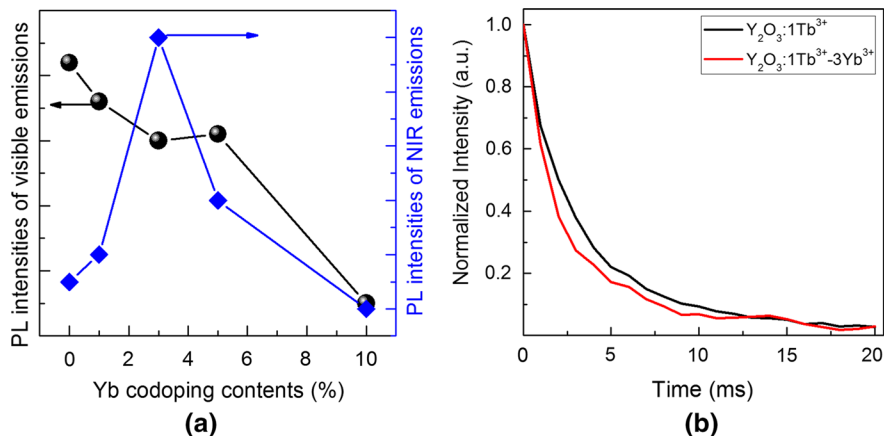
Fig. 5 Photoluminescence spectra of Y$_2$O$_3$:1 mol%Tb^{3+}–3 mol%Yb^{3+}: **a** the visible range (Tb emission) at λ_{365nm} excitation (inset: PLE spectra at λ_{547nm} emission); **b** the NIR range (Yb emission) at λ_{365nm} excitation. (Color figure online)

the same excitation condition, the green emission of Y$_2$O$_3$:Tb^{3+} was reduced and a broad NIR emission at $\lambda = 970$–1100 nm appeared. The NIR emission corresponds well to the electronic transition of Yb^{3+} ($^2F_{5/2} \rightarrow {}^2F_{7/2}$) [19] inferring the successful quantum cutting from Tb^{3+} to Yb^{3+}.

Further studies on Y$_2$O$_3$:Tb^{3+}–Yb^{3+} phosphors were conducted by varying the Yb^{3+} codoping contents, while keeping Tb^{3+} doping content at 1 mol%. Figure 6a showed relative intensities of both green and NIR emissions as a function of Yb^{3+} codoping contents (0–10 mol% in respect to Y). By increasing Yb^{3+} contents from 0 to 10 mol%, the green emission consistently decreased. In contrast, the NIR emission showed the maximum intensity with 3 mol% Yb and emission quenching was found with a further doping with 5 and 10 mol% Yb [19].

To calculate the quantum efficiency of the optimized Y$_2$O$_3$:Tb^{3+}–Yb^{3+} phosphor (doping with 1 mol% Tb and 3 mol% Yb) following the calculation method suggested by Vergeer et al. [21], decay curves of Tb^{3+} emissions were obtained for and Y$_2$O$_3$:Tb^{3+}–Yb^{3+} phosphors (Fig. 6b). The decay curve of Y$_2$O$_3$:Tb^{3+} (1 mol% Tb) showed a single exponential decay function with a decay time of ~ 2.98 ms, while that of Y$_2$O$_3$:Tb^{3+}–Yb^{3+} (1 mol% Tb and 3 mol% Yb) showed it with a decay time of ~ 2.21 ms. Supposing that the decreased decay time is due to the energy transfer from Tb^{3+} ($^5D_4 \rightarrow {}^7F_5$) to Yb^{3+} ($^2F_{7/2} \rightarrow {}^2F_{5/2}$) and there is no competing quenching process, energy transfer (ET) and quantum-cutting efficiency can be calculated as the following [5, 19]:

$$\eta_{x\%Yb} = 1 - \frac{\int I_{x\%Yb} dt}{\int I_{0\%Yb} dt}, \tag{1}$$

Fig. 6 **a** PL intensities of Y_2O_3:1 mol%Tb^{3+}–x mol%Yb^{3+} at λ_{365nm} excitation [visible (black spheres) and NIR (blue squares) emissions, individually] as a function of Yb concentrations of 0, 1, 3, 5 and 10 and **b** decay curves of Y_2O_3:1 mol%Tb^{3+} and Y_2O_3:1 mol%Tb^{3+}–3 mol%Yb^{3+} at λ_{547nm} emission. (Color figure online)

where $\eta_{x\%Yb}$ is the energy transfer of Tb → Yb at x mol% of the Yb^{3+} content and I is the intensity of decay curves. The quantum-cutting efficiency is defined by the Eq. 2 with quantum efficiencies of Tb (η_{Tb}) and Yb (η_{Yb}).

$$\eta = \eta_{Tb}\left(1 - \eta_{x\%Yb}\right) + 2\eta_{x\%Yb}. \tag{2}$$

When η_{Tb} is set to 1 assuming the energy transfer of Tb to Yb is 100%, the upper limit of quantum cutting efficiency of Y_2O_3:Tb^{3+}–Yb^{3+} (1 mol% Tb and 3 mol% Yb) is 116%. Of course, the calculated value was postulated from many assumptions, and therefore, it will be far from a measured value. However, there is a limitation in measuring the internal and external quantum efficiencies since the photon detectors used for the green and NIR regions were different.

Particle size control of Y_2O_3:1%Tb^{3+}–3%Yb^{3+} phosphors

As mentioned in the introduction session, morphology and size of flame-made particles can be tuned by the precursor conditions such as compositions and concentrations. In order to reduce the particle size down to several hundred nanometers, serial dilutions of the precursor solution with ethanol by a factor of 5 and 20 times were tried (final concentration = 0.05, 0.01 and 0.001 M). As shown in Fig. 7, the serial dilution was very effective in the particle size reduction, reaching 362 nm in avg. particle size with the precursor concentration of 0.001 M (Fig. 7c). Since the first step of FSP is the evaporation of solvent (Scheme 1), it is natural for the particle to become smaller when the precursors are diluted in solvent (the assumption here is that the droplet size is independent of precursor concentrations). However, it should be noted that it was difficult to obtain the particle size below 100 nm with a narrow
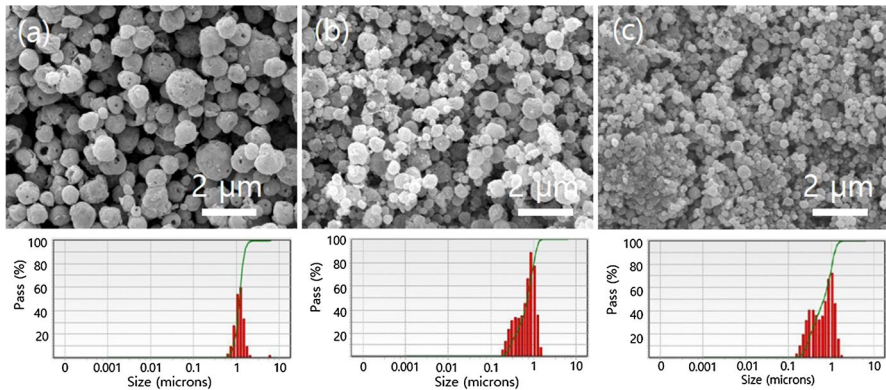
Fig. 7 SEM images and size distributions (at a magnification of ×10,000) of Y$_2$O$_3$:Tb^{3+}–Yb^{3+} synthesized with different precursor concentrations: **a** 0.05 M; **b** 0.01 M and **c** 0.001 M. (Color figure online)

size distribution by our FSP set-up because the aggregation/agglomeration of primary particles was unavoidable.

Composite films of poly-EVA and phosphors

The Y$_2$O$_3$:Tb^{3+}Yb^{3+} phosphor obtained with the precursor concentration of 0.001 M (Fig. 7c) was used to fabricate a composite film with poly-EVA matrix for a spectral convertor. The poly-EVA film was fabricated using the casting and drying method [17]. The SEM observation of the film showed that the Y$_2$O$_3$:Tb^{3+}Yb^{3+} particles are well-dispersed in the poly-EVA matrix (Fig. 8a), and the thickness of the film is about 120 μm and quite even throughout the film (Fig. 8b).

To find the optimal concentration of phosphors in the film in regards of the luminescent intensity and transparency, different amounts (1, 5, 10, and 20 mg) were used in respect to 1 g of poly-EVA. The optical transmittance and photoluminescne spectra (at λ_{365nm} excitation) of the reference poly-EVA and composite films were measured and compared in Fig. 9a and 9b, respectively. The reference film was found to be highly transparent (transmittance = ~ 93%) in both UV and visible ranges ($\lambda > 280$ nm) while a small absorption peak appeared at $\lambda = 280$ nm. The composite films showed the reduced transmittance in the UV and blue range with an increasing degree of reduction in transmittance by increasing amounts of phosphor ($0 \rightarrow 20$ mg). The transmittance reduction in the UV range ($\lambda > 350$ nm) is mainly attributed to the absorption of Y$_2$O$_3$:Tb^{3+}Yb^{3+} phosphor as shown in Fig. 5a (inset) but that in the blue range (350 nm $< \lambda <$ 500 nm) is due to the light scattering by aggregated particles. However, the transmittance of composite films, except the one with 20-mg phosphor, in the range of $\lambda > 500$ nm (where the Si solar cell responses) was as high as that of the reference film, indicating the composite films containing phosphors up to 10 mg are suitable for a spectral convertor for the Si solar cell. PL spectra of the composite films showed two PL emission ranges, green and NIR
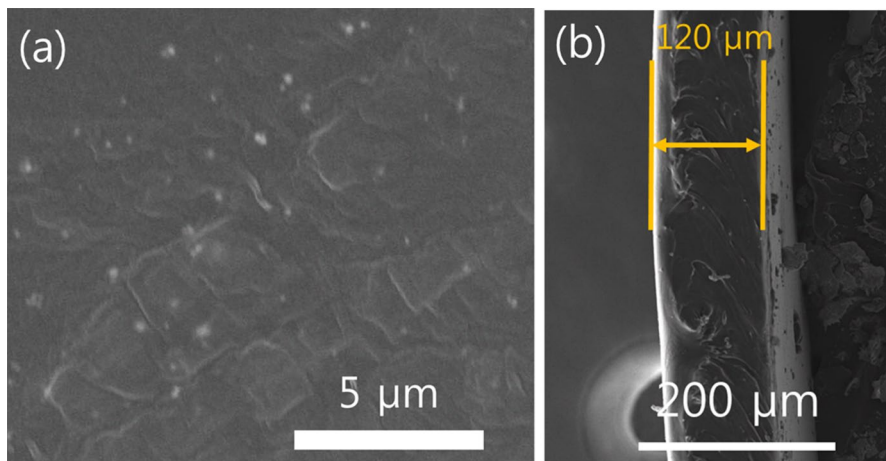
Fig. 8 SEM images of the poly-EVA film with Y_2O_3:$Tb^{3+}Yb^{3+}$ phosphor (10 mg): **a** a top view and **b** a cross-sectional view
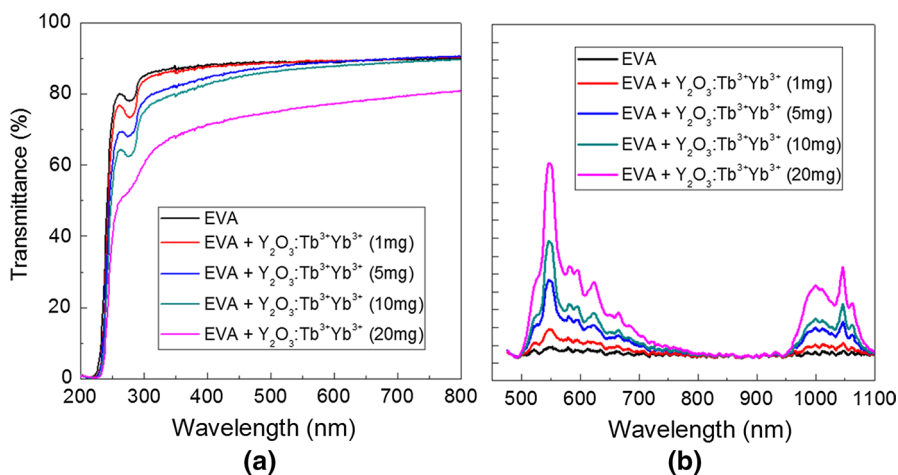
Fig. 9 **a** Optical transmittance and **b** photoluminescent spectra (at λ_{365nm} excitation) of poly-EVA films with the inclusion of different amounts of Y_2O_3:$Tb^{3+}Yb^{3+}$ (0, 1, 5, 10, and 20 mg per 1 g of poly-EVA). (Color figure online)

emissions, accounted for the luminescence of Y_2O_3:$Tb^{3+}Yb^{3+}$ phosphors. The PL intensities correlated well with contents of the phosphors in the films.

Photographic images were taken to visually compare the luminescence of the poly-EVA film with and without the phosphors. Figure 10a, b represent a reference film (without the phosphors) under natural light and a UV lamp (365 nm) and Fig. 10c, d represent a composite film with the Y_2O_3:$Tb^{3+}Yb^{3+}$ phosphor (10 mg) under natural light and an UV lamp (365 nm). The photographic images proved that
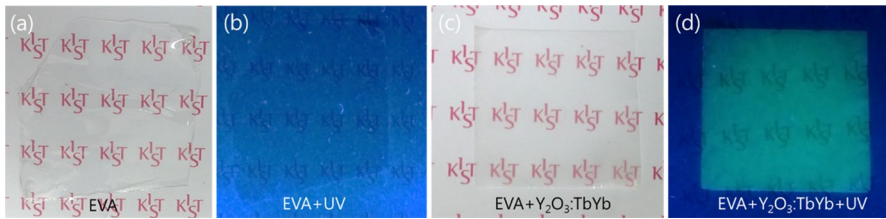
Fig. 10 Photographic images of a reference film **a** under natural light and **b** under an UV lamp (365 nm); and those of a composite film (containing 10 mg of phosphors in 1 g of polymer) **c** under natural light and **d** under an UV lamp (365 nm)

both the reference film and the composite film are quite transparent under the natural light, and the composite film emits the green color (NIR emission is not possible to observe by the naked eye) while the reference film did not luminesce (the blue color is due to the reflection of the light source). The green emission originated from the Y$_2$O$_3$:Tb^{3+}Yb^{3+} particles (more particularly, Tb^{3+} emission) embedded inside the poly-EVA film.

Conclusion

Y$_2$O$_3$:Tb^{3+}–Yb^{3+} phosphors were successfully synthesized via a continuous FSP method using methane, oxygen, and air as fuel, oxidizer, and carrier gas, respectively. Spherical particles with hollow and shell-like micro-structures, high crystallinity, and high phase purity were obtained. Particle size was controlled by managing precursor concentrations in order to provide a highly transparent spectral convertor. The phosphors exhibited green NIR emissions with a maximum quantum efficiency of ~ 116%, due to the quantum cutting phenomenon. The obtained phosphors were fabricated to serve as a spectral convertor after being embedded into a poly-EVA film and forming a composite. Transmittance of the composite film (containing up to 10 mg of phosphors in 1 g of polymer) at wavelengths above 500 nm reached over 90%, making it a good candidate for use as a spectral convertor for the Si solar cell. The composite film may be used as a thin film on top of a front glass of commercial solar cells (after careful mounting and gentle heating for adhesion) or an encapsulant between the front glass and backsheet of a solar cell.

References

1. M. Jacoby, *Chemical and Engineering News*, vol. 94 (American Chemical Society, Washington, 2016), p. 30
2. M.A. Green, K. Emery, Y. Hishikawa, W. Warta, E.D. Dunlop, Prog. Photovoltaics **24**, 3 (2016)
3. X.Y. Huang, S.Y. Han, W. Huang, X.G. Liu, Chem. Soc. Rev. **42**, 173 (2013)

4. Q.Y. Zhang, X.Y. Huang, Progr. Mater. Sci. **55**, 353 (2010)
5. A.P. Jadhav, S. Khan, S.J. Kim, S.Y. Lee, J.-K. Park, S.-H. Cho, Res. Chem. Intermed. **43**, 3463 (2017)
6. B.C. Rowan, L.R. Wilson, B.S. Richards, IEEE J. Sel. Top. Quant. **14**, 1312 (2008)
7. G. Chen, W. Qi, Y. Li, C. Yang, X. Zhao, J. Mater. Sci. Mater. Electron. **27**, 5628 (2016)
8. T. Saravanan, S.G. Raj, N.R.K. Chandar, R. Jayavel, J. Nanosci. Nanotechnol. **15**, 4353 (2015)
9. R. Strobel, S.E. Pratsinis, J. Mater. Chem. **17**, 4743 (2007)
10. W. Teoh, Materials **6**, 3194 (2013)
11. A.J. Gröhn, S.E. Pratsinis, A. Sánchez-Ferrer, R. Mezzenga, K. Wegner, Ind. Eng. Chem. Res. **53**, 10734 (2014)
12. D. Dosev, B. Guo, I.M. Kennedy, J. Aerosol Sci. **37**, 402 (2006)
13. W.N. Wang, W. Widiyastuti, I.W. Lenggoro, T.O. Kim, K. Okuyama, J. Electrochem. Soc. **154**, J121 (2007)
14. A. Camenzind, R. Strobel, S.E. Pratsinis, Chem. Phys. Lett. **415**, 193 (2005)
15. F.J. Pern, A.W. Czanderna, Sol. Energ. Mater. Sol. Cells **25**, 3 (1992)
16. H. Park, H.S. Jie, B. Neppolian, K. Tsujimaru, J.P. Ahn, D.Y. Lee, J.K. Park, M. Anpo, Top. Catal. **47**, 166 (2008)
17. W. Zhou, Y. Li, R. Zhang, J. Wang, R. Zou, H. Liang, Opt. Lett. **37**, 4437 (2012)
18. Y.C. Kang, D.J. Seo, S.B. Park, H.D. Park, Jpn. J. Appl. Phys. Pt. **1**(40), 4083 (2001)
19. J.L. Yuan, X.Y. Zeng, J.T. Zhao, Z.J. Zhang, H.H. Chen, X.X. Yang, J. Phys. D Appl. Phys. **41**, 105406 (2008)
20. L. van Pieterson, M. Heeroma, E. de Heer, A. Meijerink, J. Lumin. **91**, 177 (2000)
21. P. Vergeer, T.J.H. Vlugt, M.H.F. Kox, M.I. den Hertog, J.P.J M. van der Eerden, A. Meijerink, Phys. Rev. B **71**, 014119 (2005)